MRS Communications

https://doi.org/10.1557/s43579-022-00241-1

MRS Communications

Computational Approaches for Materials Discovery and Development Research Letter

Automated hierarchical screening of refractory multicomponent alloys with high intrinsic ductility and surface passivation potency

Aditya Sundar, Department of Materials Science and Engineering, University of Michigan, Ann Arbor 48109, USA
David Bugallo Ferron, Department of Materials Science and Engineering, Drexel University, Philadelphia 19104, USA; Centro de Investigación en Química Biolóxica e Materiais Moleculares (CIQUS), Universidade de Santiago de Compostela, 15782 Santiago, Spain
Yong-Jie Hu, Department of Materials Science and Engineering, Drexel University, Philadelphia 19104, USA
Liang Qi, Department of Materials Science and Engineering, University of Michigan, Ann Arbor 48109, USA

Address all correspondence to Liang Qi at **qiliang@umich.edu**

(Received 20 April 2022; accepted 16 August 2022)

Liang Qi was an editor of this journal during the review and decision stage. For the MRS Communications policy on review and publication of manuscripts authored by editors, please refer to http://www.mrs.org/editor-manuscripts/.

Abstract

Applications of body-centered-cubic (BCC) refractory multicomponent alloys require their room-temperature ductility and high-temperature surface passivation. Using physics-informed surrogate models and thermodynamic modeling, we devised a hierarchical workflow for the initial screening of promising refractory alloys in 13-element composition space (Ti–Zr–Hf–V–Nb–Ta–Mo–W–Re–Ru–Al–Cr–Si). Screening criteria included high intrinsic ductility according to Rice model of crack-tip deformation, pure BCC phase at 800°C, and sufficient concentrations of Cr, Al or Si for surface passivation potency. 1184 Candidates were selected from 10^7 quaternary alloys. 10 Representative candidates were verified by first-principles calculations of intrinsic ductility parameters and thermodynamic modeling of oxidation capability at 900°C.

Introduction

Body-centered cubic (BCC) refractory multicomponent alloys, including BCC refractory high entropy alloys (HEAs), are promising for use as structural components in various sectors,[1] due to their high-temperature strength and stability. Although BCC alloys possess sufficient ductility at high temperatures, e.g., 800°C, brittle mechanical behavior at lower temperatures can hinder their formability.[2,3] In addition, extreme environments encountered in energy conversion cycles, such as high-temperature and high-pressure gases,[4] and other applications can increase the risk of alloy corrosion or embrittlement. To address these materials challenges, two criteria are commonly considered for alloy selection. First, the BCC alloy must have sufficient room-temperature ductility to facilitate mechanical processing and fabrication.[1] Second, the alloy must be resistant to high-temperature oxidation and corrosion, achieved by passive oxide film formations due to alloying elements such as Al, Cr, and Si in minor concentrations.[4,5] Thus, there is a need to design accurate and efficient screening methods to guide alloy selection from the complex chemical landscape of refractory elements, with a synergistic balance between intrinsic chemical (oxide passivation) and mechanical properties (strength and ductility).

Several recent studies have been conducted to elucidate the strengthening and ductility mechanisms in BCC HEAs, spanning both multiscale computational simulations and experimental measurement of mechanical properties.[3,6] The intrinsic ductility of alloys can be well captured via several criteria such as Pugh's ratio of the bulk and shear moduli,[7] and the Rice–Thomson ratio of the stress intensities for fracture propagation and dislocation emission (so-called the Rice criterion).[8,9] An exact formulation to determine the intrinsic ductility based on the Rice criterion depends on elastic constants c_{ij}, the surface energy γ_{surf} of the cleavage fracture plane, and the unstable stacking fault (USF) energy γ_{usf} of the slip systems.[6] A simplified and efficient approach is to estimate the strength based on γ_{usf} and the intrinsic ductility based on the intrinsic ductility parameter $D = \gamma_{surf}/\gamma_{usf}$. Approximately, the yield strength enhances as the γ_{usf} increases, and a higher value of D corresponds to higher intrinsic ductility according to the Rice criterion. Both γ_{usf} and D can be computed for multicomponent solid-solution alloys based on density functional theory (DFT) calculations and special quasi-random structure (SQS) method.[10,11]

Recently, Hu et al.[12] proposed a statistical regression scheme for the rapid screening of DFT-calculated γ_{surf}, γ_{usf}, and D values of BCC refractory multicomponent alloys containing elements in Groups IV–VIII (Ti, Zr, Hf, V, Nb, Ta, Mo, W, Re, and Ru). Concisely, a model was developed to predict the composition-dependent alloy properties as a sum of individual contributions from each type of first-nearest-neighbor interatomic bond in the alloys. Here, this formalism has been

modified and extended to a wider composition space, which includes the core refractory elements and other elements (Al, Cr, and Si) that aid in high-temperature corrosion resistance by surface oxide passivation. In the first step of our hierarchical model, the DFT–SQS dataset was used to construct a regression model and sweep over a 13-element composition space with 10^7 quaternary alloy compositions to predict their γ_{usf} and D values. Based on these screening results, more than half a million candidate compositions with potentially high intrinsic ductility and moderate strengths were identified. Next, high-throughput thermodynamic calculations based on the CALPHAD (CALculation of PHAse Diagrams) method were applied to these candidates in order to determine whether it is thermodynamically possible to synthesize the single-phase BCC solid solution alloys at annealing temperatures (800°C and lower).[13] These criteria lead to 1184 quaternary alloy candidates. Finally, 10 representative candidates were selected for further verification from two aspects: the thermodynamic capability to form passive oxide films at service temperatures (900°C) using CALPHAD calculations, and the accurate values of γ_{usf}/D using DFT–SQS calculations.

Methods

DFT calculations for the dataset of γ_{surf} and γ_{usf}

The supercells to approximate random solid solution alloys in DFT calculations were generated using the SQS method as implemented in the Alloy Theoretic Automated Toolkit (ATAT).[10,14] The orthogonal unit vectors of the supercell were oriented along $0.5[111] \times [\bar{1}10] \times [11\bar{2}]$ to study γ_{usf} of the $(\bar{1}10)[111]$ slip system and γ_{surf} of the $(\bar{1}10)$ plane. Binary (with the stoichiometry of A_7B, A_3B, A_2B, AB), ternary (with the stoichiometry of ABC, A_2BC) and quaternary (with the stoichiometry of ABCD, A_2B_2CD, A_3BCD) alloy properties were calculated using a 72-atom supercell, with basis vectors along $2[111] \times 3[\bar{1}10] \times [11\bar{2}]$. Ternary compositions with the stoichiometry of A_2B_2C were modelled using a 90-atom supercell, with basis vectors along $1.5[111] \times 5[\bar{1}10] \times [11\bar{2}]$. The left subfigure in Fig. 1(a) shows the schematics for representative 72-atom bulk supercells used in our calculations, where different colors are used to represent the types of chemical elements in a multicomponent alloy. The bulk supercell has 6 interfaces between adjacent $(1\bar{1}0)$ planes labeled as Interface 1–6. The surface supercell in the center subfigure of Fig. 1(a)

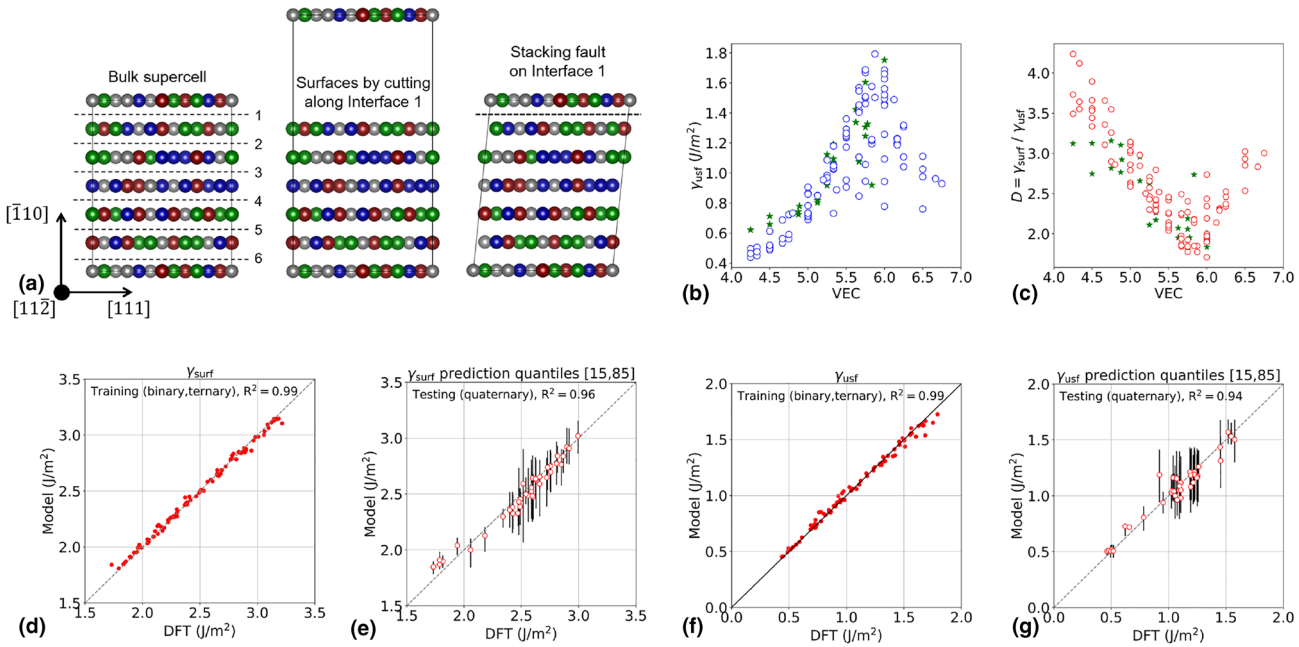

Figure 1. Dataset and performances of the surrogate models to predict γ_{usf} and $D = \gamma_{surf}/\gamma_{usf}$ based on the RFR method. (a) Alloy supercells generated by the SQS method[10] for DFT calculations to construct the dataset. The colors denote different types of chemical elements. Left subfigure: a representative bulk supercell with 6 $(\bar{1}10)$ planes (separated by Interface 1–6 plotted in dashed lines); center subfigure: a supercell for the γ_{surf} calculation generated by cutting the bulk supercell along Interface 1; right subfigure: a supercell for the γ_{usf} calculation generated by displacing the atoms above Interface 1 in the bulk supercell along $0.5[111]$ on $(\bar{1}10)$ plane. The basis vector along $[\bar{1}10]$ of the supercell is titled by $0.5[111]$ to make sure there is only one USF in this supercell. (b) γ_{usf} vs. the averaged valence electron count (VEC) for all alloys in the DFT-based dataset. (c) D vs. the averaged VEC for all alloys in the DFT-based dataset. In (b) and (c), the blue and red circles correspond to alloys that include only d-block transition elements (Ti, Zr, Hf, V, Nb, Ta, Mo, W, Re, Ru, Cr). Green stars denote alloys including Al or Si. Part of the data was obtained from a previous publication by Hu et al.[12]. (d) and (e) Training (d) and testing (e) performances for the RFR model of γ_{surf}. (f) and (g) Training (f) and testing (g) performance for the RFR model of γ_{usf}. The training sets in (d) and (f) include data from binary and ternary alloys (red dots). The testing sets in (e) and (g) include quaternary alloys (red circles). The vertical black lines in (e) and (g) denote the [15, 85] quantile from the RFR model.

contains 2 $(1\bar{1}0)$ surfaces generated by cutting along Interface 1. $\gamma_{surf} = \frac{E_{surf} - E_{bulk}}{2A}$ is the surface energy for this particular surface configuration, where E_{surf}, E_{bulk}, and A are the total energy of the surface supercell, the total energy of the bulk supercell, and the area of the $(\bar{1}10)$ plane in the supercell, respectively. The surface energy of an alloy was calculated as the average of all 6 γ_{surf} values for 6 surface supercell configurations generated by cutting along Interfaces 1–6 in a bulk supercell, respectively.

Similarly, the USF energy of an alloy was calculated as the average of 12 γ_{usf} values over all 6 interfaces between adjacent $(\bar{1}10)$ slip planes in the supercell of Fig. 1(a). 2 USF configurations were generated for each interface using 2 opposite slip directions, [111] and $[\bar{1}\bar{1}\bar{1}]$, respectively. One example supercell is plotted in the right subfigure of Fig. 1(a), which contains a stacking fault generated by a slip along [111] across Interface 1 between two adjacent $(1\bar{1}0)$ planes. The basis vector along $[\bar{1}10]$ is tilted along the slip direction to make sure there is only one stacking fault in this supercell. Thus, $\gamma_{usf} = \frac{E_{usf} - E_{bulk}}{A}$ is the USF energy for a particular combination of the slip vector and slip plane, where E_{usf} is the total energy of the supercell with a USF, approximated by a fixed displacement of $\pm 0.25[111]$ across an interface between two adjacent $(\bar{1}10)$ slip planes. Details of the calculation setup can also be found in our previous publication.[12]

In this study, γ_{surf}, γ_{usf} and D of 27 alloys (including binary, ternary and quaternary compositions) containing Al, Cr or Si in the 13-element composition space were obtained by DFT calculations. γ_{surf}, γ_{usf} and D for 106 alloys without Al, Cr or Si were directly taken from our previous publication.[12] So overall the dataset have 133 alloy compositions. All these compositions are listed in Section SI of the Supplementary Information (SI). All DFT calculations were implemented in Vienna Ab initio Simulation Package (VASP)[15] using the projected augmented wave (PAW) method.[16,17] The generalized gradient approximation was used to model the exchange-correlation energy in the formulation of Perdew, Burke, and Ernzerhof.[18] The R_k length of the automatic meshing was set to be 30 Å. The energy convergence criterion of the electronic self-consistency cycle was 10^{-6} eV for all the calculations. For the calculations of the USF and surface energies, the relaxation process was terminated when the force on each atom is less than 0.02 eV/Å. Details regarding energy convergence with respect to supercell size can be found in our previous publication.[12]

Surrogate models based on regression methods for composition screening

Surrogate models based on regression methods were implemented using the Scikit-Learn package in Python to predict values of γ_{usf}, γ_{surf}, and D of BCC refractory multicomponent alloys.[19] The final results presented in this study were generated using random forest regression (RFR) models implemented after the RFR hyperparameters were optimized by 10-fold cross-validation.[19] The Scikit-garden package was used to compute regression quantiles for the RFR model predictions.[19] Concisely, RFR is an ensemble method that is useful with sparse datasets exhibiting non-linear trends. The final ensemble model in RFR is the averaged prediction of several individual classifiers, which are called trees. Each tree is constructed by randomly selecting various sub-samples from the dataset. The number of features is also randomly selected to build each tree. Results of γ_{surf} and γ_{usf} in binary and ternary alloy supercells were used to train the RFR models, which were tested on the quaternary alloy data that were not included in the training data set. For screening purposes, the models of γ_{surf} and γ_{usf} were retrained using the entire 133 alloy dataset with the same hyperparameters and features. The selection of features and the construction of descriptors of these RFR models are discussed in the following.

Physical properties of an alloy can be approximated by the collective contributions from certain characteristics and feature parameters of each interatomic bond in the alloy.[12] If only the first-nearest-neighbor interatomic bonds are considered in a random alloy, the probability of an i–j bond between elements i and j is equal to the product of their mole fractions. Building on this bond-counting scheme, general surrogate models to predict the physical properties of alloys can be formulated to consider information about the global alloy composition and the characteristics of every i–j bond found in that alloy. Recently, Hu et al.[12] have shown the effectiveness of such surrogate models in predicting the γ_{usf} and D parameters of BCC alloys containing the core refractory elements in Groups IV–VIII. Here, we adopt those surrogate models with a new set of interatomic bond feature parameters and regression methods to accommodate the characteristics of p-block elements such as Al and Si. Then these surrogate models are applied to screen over a wider 13-element composition space.

The next few paragraphs discuss procedures to use these bond features to construct the descriptors as the inputs of surrogate models for composition-dependent alloy properties. For any bond feature parameter p_{ij} of the i–j bond between elements i and j, the corresponding alloy descriptor u_p and the corresponding weighted deviation u_p^σ are defined as the follows

$$u_p = \sum_i x_i \sum_j x_j p_{ij}, \tag{1}$$

$$u_p^\sigma = \sqrt{\left(\frac{1}{1-\sum_i x_i^2}\right) \times \left(\sum_i x_i \left(\sum_j x_j p_{ij} - u_p\right)^2\right)}, \tag{2}$$

where x_i denotes the mole fraction of element i among 13 elements in the alloy. The summations in Eqs. (1) and (2) include all i–j first-nearest-neighbor interatomic bonds between elements i and j in the alloy. All values of p_{ij} can be written as a 13×13 matrix. The matrix elements p_{ij} are obtained from DFT calculations of certain properties of pure metals in both BCC lattice and its corresponding ordered binary alloys in the B2 structure. So these bond feature parameters are denoted as $p_{ii}^{BCC/B2}$. In addition, to consider the bond features in other

lattice structures that could be critical to certain elements such as Al, another group of p_{ij} values is also obtained from DFT calculations of properties of pure metals in both FCC lattice and its corresponding ordered binary alloys in the $L1_0$ structure. So these bond feature parameters are denoted as $p_{ij}^{FCC/L1_0}$.

Specifically, any property p of BCC pure metals is attributed to i–i bond features as $p_{ii}^{BCC/B2}$. A 2-atom B2 supercell, which has one atom of element i and one atom of element j, contains only 8 i–j first-nearest-neighbor interatomic bonds so that its property p can be attributed to i–i bond features as $p_{ij}^{BCC/B2}$. Similarly, any property p of FCC pure metals can be attributed to i–i bond features as $p_{ii}^{FCC/L1_0}$. However, a 4-atom $L1_0$ supercell contains effectively 4 i–i, 4 j–j and 16 i–j first-nearest-neighbor bonds. For a rigorous attribution of any $L1_0$ property p into its bond constituents, the contributions of $p_{ii}^{FCC/L1_0}$ and $p_{jj}^{FCC/L1_0}$ to p should be removed based on the simple linear relation as Eq. (1) to obtain the i–j bond feature as $p_{ij}^{FCC/L1_0}$. Nevertheless, as an approximation (since two-thirds of the bonds in $L1_0$ are of type i–j), some $p_{ij}^{FCC/L1_0}$ here are directly obtained from the corresponding p value for the whole $L1_0$ supercell. Detailed descriptions for the calculation of feature parameter matrices and descriptors are provided in Sect. SII of the SI.

Table I. Feature parameters and descriptors of random forest regression (RFR) models of γ_{surf} and γ_{usf}.

Descriptor name	Descriptor notation (u_p)	Calculation from feature parameter p
Surface energy	$\gamma_{surf}^{BCC/B2}$	$\sum_i x_i \sum_j x_j \gamma_{surf,ij}^{BCC/B2}$
Unstable stacking fault energy	$\gamma_{usf}^{BCC/B2}$	$\sum_i x_i \sum_j x_j \gamma_{usf,ij}^{BCC/B2}$
Volume per atom	$V^{BCC/B2}$	$\sum_i x_i \sum_j x_j V_{ij}^{BCC/B2}$
	$V^{FCC/L1_0}$	$\sum_i x_i \sum_j x_j V_{ij}^{FCC/L1_0}$
Bond length	$\lambda^{BCC/B2}$	$\sum_i x_i \sum_j x_j \lambda_{ij}^{BCC/B2}$
	$\lambda^{FCC/L1_0}$	$\sum_i x_i \sum_j x_j \lambda_{ij}^{FCC/L1_0}$
Cohesive energy per atom	$E_{coh}^{BCC/B2}$	$\sum_i x_i \sum_j x_j E_{coh,ij}^{BCC/B2}$
	$E_{coh}^{FCC/L1_0}$	$\sum_i x_i \sum_j x_j E_{coh,ij}^{FCC/L1_0}$
Moments of the PDOS	$\epsilon_n^{BCC/B2}$	$\sum_i x_i \sum_j x_j \epsilon_{n,ij}^{BCC/B2}$
	$\epsilon_n^{FCC/L1_0}$	$\sum_i x_i \sum_j x_j \epsilon_{n,ij}^{FCC/L1_0}$
Integrated PDOS	$n_{s/p/d}^{BCC/B2}$	$\sum_i x_i \sum_j x_j n_{s/p/d,ij}^{BCC/B2}$
	$n_{s/p/d}^{FCC/L1_0}$	$\sum_i x_i \sum_j x_j n_{s/p/d,ij}^{FCC/L1_0}$
Valence electron count from pseudopotential	VEC	$\sum_i x_i \mathrm{VEC}_i$
Electronegativity	χ	$\sum_i x_i \chi_i$

The table lists the set of descriptors u_p based on alloy/metal properties p in its second column and the corresponding feature parameters in its third column, which include the feature parameters ($p_{ij}^{BCC/B2}$ and $p_{ij}^{FCC/L1_0}$) of the first-nearest-neighbor bond between element i and j and the element properties (p_i). x_i/x_j is the mole fraction of element i/j in the alloys.

Table I lists the alloy descriptors (u_p) used in our model, along with their specific notations and their calculation methods from the corresponding feature parameter p_{ij}. Two of the descriptors are estimations of the surface energy and USF energy of multicomponent alloys based on their counterparts in pure BCC metals and ordered B2 alloys. These descriptors have the notations $\gamma_{surf}^{BCC/B2}$ and $\gamma_{usf}^{BCC/B2}$, respectively. Diagonal elements in the corresponding feature parameter matrices of the 13 elements are denoted $\gamma_{surf,ii}^{BCC/B2}$ and $\gamma_{usf,ii}^{BCC/B2}$, respectively, whose values are obtained from DFT calculations for unary BCC structures containing surface and USF configurations. The corresponding off-diagonal matrix elements $\gamma_{surf,ij}^{BCC/B2}$ and $\gamma_{usf,ij}^{BCC/B2}$ are obtained from DFT calculations for ordered B2 structures containing surface and USF configurations. The DFT supercells in these calculations are similar to the description in "DFT calculations for the dataset of γ_{surf} and γ_{usf}" section and illustration in Fig. 1(a), but with reduced multiplicity along [111] due to the higher symmetry of BCC/B2 structures. The corresponding weighted deviation associated with each descriptor is calculated using Eq. (2) and is also included as a descriptor in our model.

Another descriptor in Table I is the volume per atom calculated for both BCC and FCC polymorphs. Their notations are $V^{BCC/B2}$ and $V^{FCC/L1_0}$. The diagonal elements of the feature parameter matrix of the 13 elements $V_{ii}^{BCC/B2}$ are obtained from DFT calculations for a conventional 2-atom BCC supercell. The off-diagonal elements $V_{ij}^{BCC/B2}$ are obtained from DFT calculations for a 2-atom ordered B2 supercell. Analogously, the diagonal elements $V_{ii}^{FCC/L1_0}$ are obtained from DFT calculations for a conventional 4-atom FCC supercell and the off-diagonal elements $V_{ij}^{FCC/L1_0}$ are obtained from DFT calculations for a conventional 4-atom ordered $L1_0$ supercell. Totally, there are 4 volume descriptors as seen from Eqs. (1) and (2). These include the volume per atom for BCC/B2, the volume per atom for FCC/$L1_0$ and their corresponding weighted deviations. Other structure-specific descriptors include bond length for the BCC/B2 and FCC/$L1_0$ structures ($\lambda^{BCC/B2}$ and $\lambda^{FCC/L1_0}$, respectively) and cohesive energy per atom ($E_{coh}^{BCC/B2}$ and $E_{coh}^{FCC/L1_0}$, respectively). Cohesive energies are calculated with respect to the isolated atom reference states. Notations of their corresponding elements of the feature parameter matrices are tabulated in Table I.

Table I also shows descriptors constructed using the projected electronic density of states (PDOS) since our previous studies show the descriptors of local electronic structure can be used to predict the defect properties in BCC refractory metals.[20] The first, second, third and fourth moments of the PDOS are denoted as $\epsilon_n^{BCC/B2}$ and $\epsilon_n^{FCC/L1_0}$, where n is the order number from 1 to 4. The PDOS includes contributions from individual s, p and d orbitals (note that the d contribution to Al and Si is zero), so the orbital resolved integrated PDOS is also included in our model, denoted as $n_{s/p/d}^{BCC/B2}$ and $n_{s/p/d}^{FCC/L1_0}$. These quantities are also calculated using the 2-atom supercells for BCC/B2 and 4-atom supercells for FCC/$L1_0$ structures.

Detailed descriptions for the calculation of their feature parameter matrices are provided in Sect. SII of the SI.

In addition to the properties of pure metals and ordered alloys discussed in the above paragraph, element-specific properties, such as electronegativity (χ) and the valence electron count (VEC) of each element, were also used to construct the descriptors. For any multicomponent alloy, the corresponding descriptors include the concentration averaged element-specific properties and their weighted deviations defined as

$$u_p = \sum_i x_i p_i, \tag{3}$$

$$u_p^{\sigma} = \sqrt{\left(\frac{1}{1-\sum_i x_i^2}\right) \times \left(\sum_i x_i \left(p_i - u_p\right)^2\right)}. \tag{4}$$

Here p_i is the χ or VEC of element i for each of 13 investigated elements.

With all the above descriptors, two separate RFR models were developed to fit the γ_{surf} and γ_{usf} data, respectively. Overall, there are 23 types of descriptors considered for each RFR model list as follows: 1 descriptor based on the planar fault energy ($\gamma_{surf}^{BCC/B2}$ or $\gamma_{usf}^{BCC/B2}$), 2 descriptors based on the cohesive energy per atom ($E_{coh}^{BCC/B2}$ and $E_{coh}^{FCC/L1_0}$), 2 descriptors based on the volume per atom ($V^{BCC/B2}$ and $V^{FCC/L1_0}$), 2 descriptors based on the bond length ($\lambda^{FCC/L1_0}$ and $\lambda^{BCC/B2}$), 8 descriptors based on moments of the PDOS ($\epsilon_n^{BCC/B2}$ and $\epsilon_n^{FCC/L1_0}$, $n = 1, 2, 3, 4$), 6 descriptors based on integrated PDOS of individual s, p, and d orbitals ($n_{s/p/d}^{BCC/B2}$ and $n_{s/p/d}^{FCC/L1_0}$), 1 descriptor based on the electronegativity χ, and 1 descriptor based on VEC. For a given alloy, each descriptor [denoted as u_p in Eqs. (1) and (3)] is obtained by computing the concentration-averaged feature parameters [denoted as p_{ij} in Eqs. (1) and (3)]. In addition, there is one weighted deviation value for each descriptor, denoted as u_p^{σ} in Eqs. (2) and (4). All the descriptors and their feature parameters are tabulated in Table I. The weighted deviations for the element-specific properties χ and VEC were found to reduce model accuracy and were not included in the final model. Thus, there are totally $(23 \times 2 - 2) = 44$ descriptors for each RFR model.

CALPHAD models for phase diagram calculations

The Thermo-Calc[21] software was used for thermodynamics calculations as implemented in the CALPHAD method.[22] In brief, the Gibbs free energy of the total system is minimized to obtain phase amounts and compositions at equilibrium as a function of global thermodynamic variables (temperature, pressure, and composition).[22] Alloy phase diagrams were calculated using the Thermo-Calc Software TCHEA High Entropy Alloys database version 4 (TCHEA4). To assess the phase equilibrium and thermodynamic driving force associated with surface oxidation, TCHEA4 was combined with Thermo-Calc Software SSUB General Alloys and Pure Substances version 6 (SSUB6).

Results and discussion

DFT calculations of surface energies and stacking fault energies

As outlined in "DFT calculations for the dataset of γ_{surf} and γ_{usf}" section, γ_{surf} and γ_{usf} were calculated using the DFT–SQS method applied to supercells illustrated in Fig. 1(a). As explained in "DFT calculations for the dataset of γ_{surf} and γ_{usf}" section, the value of $\gamma_{surf}/\gamma_{usf}$ for each alloy are obtained from 6/12 calculations of different surface/USF supercell configuration. Section SIII of the SI show detailed results of $\gamma_{surf}/\gamma_{usf}$ for each supercell configurations of certain selected alloys that contain Al, Cr, or Si. Figure 1(b) and (c) show γ_{usf} and $D = \gamma_{surf}/\gamma_{usf}$ of an alloy plotted against the composition averaged VEC of this alloy for all cases calculated by the DFT–SQS method. The average VEC is given as $\sum_i x_i \mathrm{VEC}_i$, where x_i is the molar composition of the alloy and VEC_i is the number of valence electrons per atom for the element type i. The data shows a general trend that the highest values of γ_{usf} and the lowest values of D usually appear in the alloys with VEC ≈ 6, indicating general strength–ductility trade-off.[12] These trends are generally consistent with the facts that (1) Group VI metals (such as W and Mo) have the highest hardness but are brittle, and (2) the intrinsic ductility of BCC refractory alloys is strongly correlated to the d-band filling.[23] However, there are still scattered distributions of γ_{surf} and D even for alloys with the same VEC values, suggesting the necessity to design accurate predictive models based on feature parameters of chemical and electronic properties besides the VEC values.

Surrogate model performance

Ensemble methods such as RFR are useful when the target property shows linear and/or non-linear dependencies on the descriptors. For instance, in our study, the γ_{surf} property shows roughly linear dependence on the $\gamma_{surf}^{BCC/B2}$ descriptor (defined earlier in Table I). However, there are non-linear dependencies on other descriptors in Table I, such as VEC, $\lambda^{BCC/B2}$, $n_{s/p/d}^{BCC/B2}$, etc. Similar observations are made for the γ_{usf} property. These dependencies are shown in Sect. SIV of the SI. Using relatively simple regression models results in poor predictive accuracy, especially for γ_{usf}. Therefore, the RFR method was chosen for the final model in this work.

The performances of RFR models for γ_{surf} and γ_{usf} prediction are summarised in Fig. 1(d)–(g). Figure 1(d) shows the DFT calculated γ_{surf} plotted against the model output for samples in the training set. Here, the training set includes all binary and ternary alloy data. Figure 1(e) shows the performance of the trained RFR model of γ_{surf} for the testing set containing all quaternary compositions. Similarly, Fig. 1(f) and (g) show training (binary and ternary alloys) and testing (quaternary alloys) results for the RFR model of γ_{usf}. The black vertical lines in Fig. 1(e) and (g) denote the [15, 85] prediction quantiles. Even though the models in Fig. 1(d) and (f) were trained on binary and ternary compositions, the testing results in Fig. 1(e) and (g) show good accuracy with $R^2 = 0.96$ and 0.94, respectively. Both the training and

testing datasets cover a similar range for $\gamma_{surf}/\gamma_{usf}$, with a lower bound of around 1.75/0.5 J/m^2 and an upper bound of around 3.25/1.65 J/m^2, respectively.

Comparing with the RFR model for γ_{surf}, the RFR model for γ_{usf} is less accurate, with slightly larger values of R^2 and quantiles. The root mean squared error for both γ_{surf} and γ_{usf} predictions is ~ 0.07 J/m^2. However, lower absolute values for γ_{usf} results in comparatively poor accuracy. One possible reason could be the inaccurate approximation of *i*–*j* bond feature parameters in FCC structure as the properties for ordered alloys in the $L1_0$ structure as described previously in "Surrogate models based on regression methods for composition screening" section. In the future, this approximation will be addressed to develop more accurate feature parameters and descriptors. In addition, analyses of all the descriptors of the RFR models show that the $\gamma_{surf}^{BCC/B2}/\gamma_{usf}^{BCC/B2}$, all the descriptors related to PDOS, and the composition averaged VEC and electronegativity χ are features with the highest importance and correlations. It indicates that the first-nearest-neighbor bond model with electronic and energetic feature parameters developed in our previous work[12,20] are generally accurate for the target alloy properties, which can possibly be extended to other properties in the future.

Hierarchical screening framework

Using the RFR-trained surrogate models, a 5-step hierarchical screening framework is designed to identify candidate alloys with targeted strength, ductility, and corrosion resistance properties. The screening method is summarised in Fig. 2(a). Details for each screening step are discussed in the following.

First, the surrogate models described in "Surrogate models based on regression methods for composition screening" and "Surrogate model performance" sections are used to screen all possible quaternary alloys within the 13-element composition space under the following constraints. The maximum composition of any element is restricted to less than 60%. The screening search is implemented in composition steps of 1/72, since most DFT supercells in our setup have 72 atoms. However, it is technically possible to make predictions for any arbitrary composition and then validate results using appropriate DFT supercell setups. Initially, the average alloy descriptors $[u_p, u_p^\sigma$ from Eqs. (1) to (4)] for each composition are generated following the method discussed in "Surrogate models based on regression methods for composition screening" section. Next, γ_{surf} and γ_{usf} predictions are made using the surrogate models with u_p and u_p^σ as inputs. These screening results are summarised in Fig. 2(b), where γ_{usf} is plotted against D for 10,376,496 quaternary compositions. These compositions are obtained with the constraints that (1) the composition x of every element is varied in a step of $\frac{100}{72}$ %, (2) $x_{Ru} < 5\%$, (3) $x_{Al} < 15\%$, (4) $x_{Si} < 5\%$, and (5) the maximum concentration of any element in an alloy is 60% (all percentages are for the mole fraction). The red reference markers in Fig. 2(b) are the DFT calculated values for pure refractory metals in the BCC structure. Group VI elements (Cr, Mo, W) are the strongest with the highest $\gamma_{usf} \sim 1.4$–1.6 J/m^2 but brittle with $D \sim 2$. Group V elements (V, Nb, Ta) are relatively soft with the reduced $\gamma_{usf} \sim 0.7$–0.8 J/m^2 but more ductile with $D \sim 3$–3.5. Pure metals of other elements have dynamical structural instabilities in the BCC phase, so their γ_{usf} and D are not plotted here.

Second, compositions are selected with relatively high values of the intrinsic ductility parameter D. The general strength–ductility trade-off in Fig. 2(b) indicates it is difficult to find a single BCC phase with both high values of γ_{usf} and D. So our strategy is to discover some single BCC phase candidates with high intrinsic ductility and moderate strengths. These single-BCC-phase alloys can serve as the matrix, and the alloys can be further strengthened by the addition of primary or secondary precipitate phases to the BCC matrix.[1] Our previous calculations of D values of many experimentally synthesized BCC refractory multicomponent alloys suggest that the high room-temperature ductility is more likely to be achieved in alloys with D values larger than 3,[12] which are consistent with D values of Group V elements. In addition, the values of γ_{usf} can not be too low for structural applications. These requirements constrain our selection region in a rectangle highlighted in Fig. 2(b), where $3.0 < D < 3.5$ and $0.6 < \gamma_{usf} < 0.8$ J/m^2. Furthermore, we require the total mole fraction of all Group V and VI elements in these alloys to be at least 50% in order to increase the likelihood of the synthesis of single-BCC-phase alloys. Under these requirements, a total of 587,184 candidate alloys are selected in this step for further CALPHAD analyses on phase stability.

Third, high-throughput CALPHAD calculations of 587,184 alloy candidates are performed to search alloy compositions that can be in a single BCC phase at the typical annealing temperatures of refractory metals,[13] using the TC-Python API.[21,24] We remark here that phase diagram data are successfully computed for $\sim 540,000$ alloys or $\sim 92\%$ of the compositions screened after the second step. Errors for the remaining 8% compositions could arise from database calibration or the TC-Python API timeout. Phase diagrams for these specific compositions will be generated manually in the future. Then these candidate alloys are selected based on the following two criteria: (i) there is greater than 99.99% BCC phase purity at 800°C, a typical annealing temperature of refractory metals,[13] and (ii) $10\% \le x_{Al} + x_{Cr} + x_{Si} \le 20\%$. The constraint on Al, Cr, and Si concentrations increases the likelihood of thermodynamic surface oxide formation capability. These results are shown in Fig. 2(c). Cumulative bar plots at each temperature show the total number of selected composition candidates. At 800°C, 1184 alloy compositions are identified within the imposed two constraints, but none of them contain Si. We can further explore whether it is possible to keep the single BCC phase at lower annealing temperatures. Results show that there are still hundreds of alloy candidates in almost single BCC phase and with at least 10% of Al and Cr in the temperature range of 550 to 750°C. Finally, at 500°C, none of the alloys have the BCC phase purity due to the appearance of precipitate phases such as the Laves phase. Alternatively, Fig. 2(d) plot

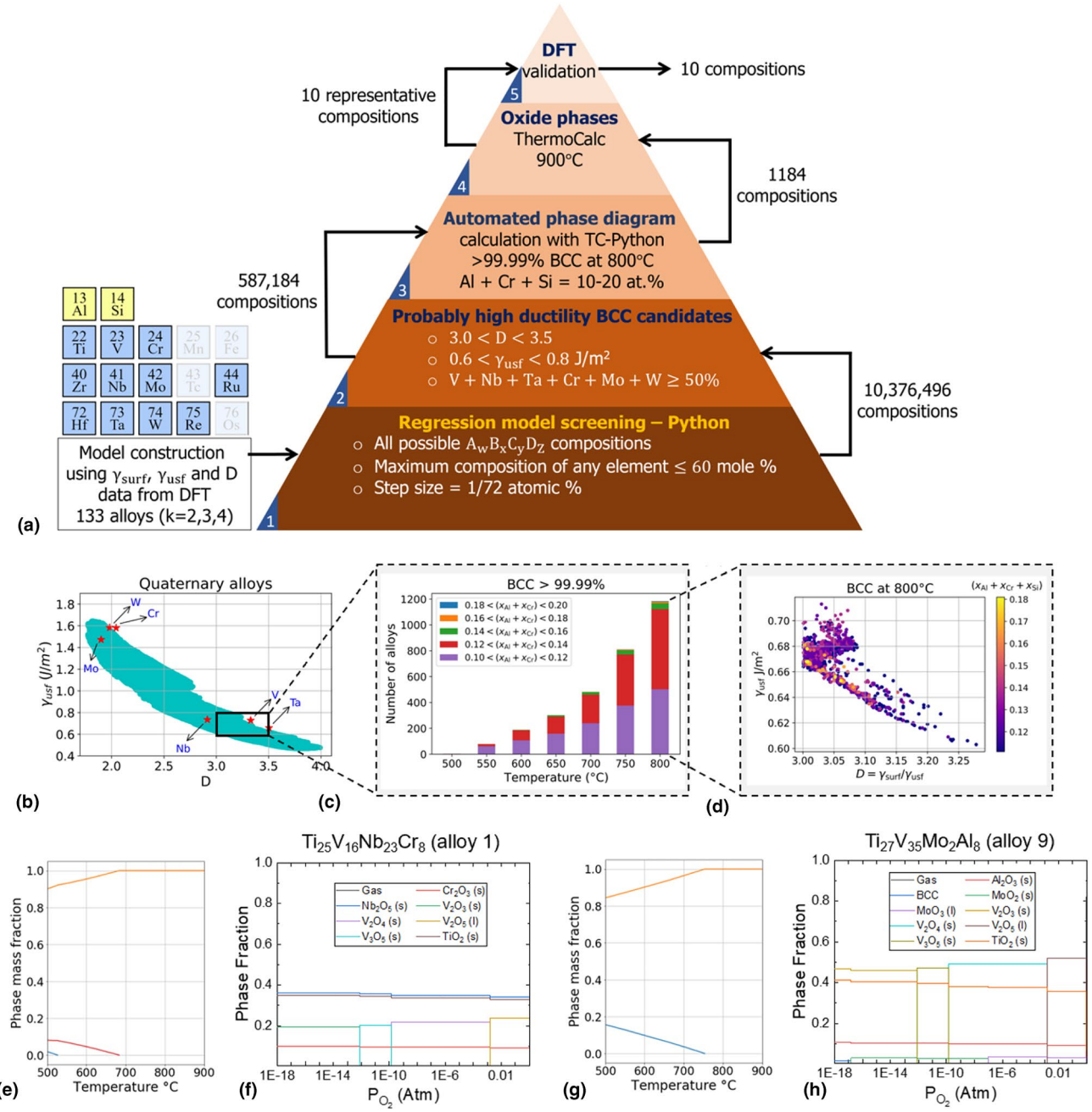

Figure 2. Illustration of the hierarchical screening model and its results. (a) A multi-level pyramid to explain the 5-step model based on DFT calculations, RFR models, and CALPHAD method. Each level of the pyramid summarises the corresponding screening procedure. Detailed descriptions are provided in "Hierarchical screening framework" section. Input arrows denote the number of input compositions. Output arrows denote the number of screened/filtered output compositions. The partial periodic table and accompanying text on the left depict the RFR models of γ_{usf}, γ_{surf}, and D, which are used to screen alloys in Step 1. (b) Screening results of γ_{usf} and D of over 10^7 quaternary compositions in the 13-element composition space (Step 1). The black rectangle borders the region of interest (587,184 compositions from 10,376,496 candidates from Step 2). (c) Results from the CALPHAD-based phase diagram calculations (Step 3). 1184 Compositions from 587,184 candidates have > 99.99% BCC at 800°C with $10\% < x_{Al} + x_{Cr} < 20\%$, where x denotes the mole fraction. No alloys with Si elements are found in this step. (d) The distributions of γ_{usf} and D for 1184 alloy compositions from (c), with the color scale corresponding to the total mole fraction of Al, Cr and Si of each alloy candidate. (e)–(h) CALPHAD calculations for representative alloy candidates. (e) Equilibrium phase fractions for $Ti_{25}V_{16}Nb_{23}Cr_8$ at different temperatures. (f) Equilibrium phase fractions of oxides formed from $Ti_{25}V_{16}Nb_{23}Cr_8$ at 900°C under different oxygen partial pressures. (g) Equilibrium phase fractions or $Ti_{27}V_{35}Mo_2Al_8$ at different temperatures. (h) Equilibrium phase fractions of oxides formed from $Ti_{27}V_{35}Mo_2Al_8$ at 900° C under different oxygen partial pressures. Data in (e) and (g) was obtained using the TCHEA4 database. Data in (f) and (h) was obtained using the TCHEA4 + SSUB6 databases. In plots (e)–(h), the left axis is mole fraction.

Table II. DFT validations for representative alloy candidates.

	ID	Alloy	γ_{surf} (J/m^2)		γ_{usf} (J/m^2)		$D = \frac{\gamma_{surf}}{\gamma_{usf}}$	
			DFT	Model	DFT	Model	DFT	Model
Cr	1	$Ti_{25}V_{16}Nb_{23}Cr_8$	2.034	1.996	0.628	0.651	3.241	3.067
	2	$Ti_{25}V_{20}Nb_{19}Cr_8$	2.036	2.003	0.647	0.664	3.149	3.017
	3	$Ti_{32}V_{10}Nb_{22}Cr_8$	1.967	1.978	0.643	0.603	3.060	3.278
	4	$Ti_{35}V_{24}Mo_5Cr_8$	2.067	2.062	0.673	0.686	3.071	3.007
Al	5	$Ti_{27}V_{24}Mo_{13}Al_8$	2.071	2.091	0.752	0.686	2.754	3.048
	6	$Ti_{18}V_{41}Re_3Al_{10}$	2.102	2.103	0.708	0.689	2.971	3.054
	7	$Ti_{26}V_{31}Mo_6Al_9$	2.069	2.053	0.716	0.675	2.891	3.042
	8	$Ti_9V_{31}Nb_{22}Al_{10}$	2.040	1.999	0.710	0.665	2.873	3.007
	9	$Ti_{27}V_{35}Mo_2Al_8$	2.051	2.024	0.642	0.667	3.195	3.035
Al + Cr	10	$Ti_{30}V_{32}Al_5Cr_5$	2.036	2.012	0.703	0.636	2.897	3.161

The tabulated values show RFR-model-predicted and DFT-calculated γ_{surf}, γ_{usf}, and D parameters for 10 representative alloy candidates. This set includes 4 alloys with Cr, 5 with Al and 1 with both Cr and Al.

both the distributions of γ_{usf} and D of 1184 alloy candidates with the pure BCC phase at 800°C and the color scale corresponding to the total mole fraction of Al, Cr, and Si.

At the final two steps, 10 representative candidates are selected from the above 1184 alloy compositions for further verification from two aspects: the thermodynamic capability to form passive oxide films at possible service temperatures (900°C used here) using CALPHAD calculations, and the accurate values of γ_{usf}/D using the DFT–SQS method. The compositions of 10 representative candidates are listed in Table II. These alloys are selected from different regions of the screened plot in Fig. 2(d). Eight of the ten alloys are selected from the dense cluster near the top left region in Fig. 2(d), where $3.0 < D < 3.1$. One alloy is selected from the intermediate region where $3.1 < D < 3.2$, and one from the bottom right region with $3.2 < D < 3.3$. Alloys 1, 2, 3 and 8 in Table II include core elements from Groups IV and V, along with the oxide-forming elements Cr or Al. Alloys 4, 5, 7 and 9 in Table II include core elements from Groups IV, V and VI, along with Cr or Al. Alloy 6 has a small amount of Re, which is useful to enhance ductility but added in minor concentrations due to its high economic costs. Alloy 10 includes Al and Cr in equal amounts. Overall, five of these alloys contain Al, four contain Cr, and one contains both Cr and Al. No compositions with Si are found after the multiple screening steps. All these alloys are rich in Group IV, V, and VI elements (significant concentrations of Ti, V, and Nb), and contain varying amounts of Nb, Mo, and Re.

Table II also lists the ML-predicted and DFT–SQS-computed parameters of γ_{surf}, γ_{usf} and D for the 10 representative candidates. Detailed DFT–SQS results of the 10 representative candidates are shown in Sect. SV of the SI. Generally, the DFT results are consistent with our RFR model predictions with the accuracy on the same level shown in Fig. 1(d)–(g). Meanwhile, the model for γ_{usf} is less accurate than the model for γ_{surf}, especially for alloys containing Al. It suggests that we can improve the predictions by more accurate descriptions of bond feature parameters that involve elements with FCC and other non-BCC stable structures.

Phase fractions at varying temperatures for two alloys of these 10 representative candidates ($Ti_{25}V_{20}Nb_{19}Cr_8$ as Alloy 1 and $Ti_{27}V_{35}Mo_2Al_8$ as Alloy 9 in Table II) are shown by phase diagrams in Fig. 2(e) and (h). These phase diagrams confirm that these alloys have more than 99.99% BCC phase at 800°C. At lower temperatures, other precipitate phases, such as Laves or $AlTi_3$, can be thermodynamically stable. In addition, adopting the method used in recent literature,[25] phase fractions of these two alloys in oxidation environments were illustrated by phase diagrams at 900°C by varying the oxygen partial pressure in Fig. 2(f) and (h), which show that several oxides can be thermodynamically stable at 900°C, including titania, alumina, chromia, and vanadia, covering multiple stoichiometries.

We also calculate the thermodynamic driving force for the oxidation of each metallic element in the alloys at 900°C (details in Sect. SVI of the SI), adopting the method used in recent literature.[26] The results show that, among all metallic elements in each alloy of Alloys 1–4 in Table II, Ti has the largest thermodynamic driving force for its oxidation by forming TiO_2, followed by Nb_2O_5, V_2O_4 and Cr_2O_3. For Alloys 5–10 in Table 2II, Ti and Al have the largest and the second largest thermodynamic driving force for oxidation, forming TiO_2 and Al_2O_3, respectively. Since both Ti and Al alloying elements can form effective passive oxide films for refractory alloys,[5] these results suggest that these candidate alloys possibly have strong oxidation and corrosion resistance. However, the chemical compositions and other properties of real passive oxide layers will also be determined by kinetic factors, which can not be obtained from equilibrium phase diagrams alone.

Conclusion

In summary, we have proposed a hierarchical screening workflow to identify BCC refractory multicomponent alloys potentially with synergistic mechanical properties and chemical stability. A regression model developed using a sparse DFT-based dataset was used to predict the surface energy γ_{surf} and the

USF energy γ_{usf} for quaternary alloys in 13-element composition space (Ti–Zr–Hf–V–Nb–Ta–Mo–W–Re–Ru–Al–Cr–Si). Further screening was performed to discover candidate alloys satisfying the following criteria: (1) the strength parameter γ_{usf} and the intrinsic ductility parameter $D = \frac{\gamma_{surf}}{\gamma_{usf}}$ are comparable to Group V metals (V, Nb, and Ta) for moderate strengths and high room-temperature ductility/formability, (2) there is more than 99.99% BCC phase at 800°C, and (3) there are 10–20 mole% of oxide-forming elements (Cr, Al and Si) for high-temperature surface passivation. CALPHAD-based thermodynamics calculations were used to confirm BCC phase stability at 800°C. After a multiple-step screen, we found 1184 alloy compositions that satisfy all these criteria. 10 representative candidates were chosen from these alloys for further investigations. CALPHAD-based thermodynamics calculations were then applied to calculate the thermodynamic oxide formation capability at 900°C, suggesting the possibility of passive oxide layer formations on these representative candidates. DFT validations for γ_{surf}, γ_{usf} and D further confirmed that the representative candidates have $D >\sim 3$, which is the targeted value for BCC refractory multicomponent alloys to possibly reach high room-temperature ductility.[12]

It is important to remark here that the strength and ductility of alloys are strongly influenced by other factors such as additional deformation systems,[6] interstitial impurities, secondary precipitate phases and other microstructural constituents (grain size, morphology, etc.).[27] Additional considerations are also crucial to study the stability of passive oxides. While CALPHAD-based calculations used in this work show the thermodynamic capability of passive oxide formation, several other factors can influence oxide stability in reactive environments. These include elemental diffusion in the metal matrix and oxide, lattice mismatch between the metallic alloys and oxide,[28] thermal expansion mismatch between the metallic matrix and the oxide film,[29] etc. In addition, brittle inclusions such as carbides within the matrix especially close to the oxide layers can also promote crack initiation on the metal–oxide interface and result in oxide layer spallation.[29] Within these broad challenges of alloy design, the workflow devised in this paper is intended to enable the initial selection of promising high-ductility single-phase compositions based on relatively simple but rapid screening criteria. Additional thermomechanical properties, such as elastic constants, grain boundary energetics, impacts of interstitial segregation on fracture mechanisms, Pilling–Bedworth ratio, thermal expansion coefficients and other microstructural descriptors can then be computed using multiscale methods,[6,30] to develop a more rigorous description of the intrinsic mechanical and chemical properties in multicomponent refractory alloys.

Acknowledgments

A. S. and L. Q. acknowledge the financial supports from the National Science Foundation (NSF) Award DMR-1847837 and Michigan Materials Research Institute (MMRI) Seed Fund. Y. J. H. acknowledge the financial supports from the Startup Fund from Drexel University. D. B. acknowledges financial support through the Program for the Requalification, International Mobility and Attraction of Talent in the Spanish University System, Modality Margarita Salas. The calculations were performed by using the Extreme Science and Engineering Discovery Environment (XSEDE) Stampede2 at the TACC through Allocation TG-DMR190035. This research was supported in part through computational resources and services provided by Advanced Research Computing Technology Services (ARC-TS), a Division of Information and Technology Services (ITS) at the University of Michigan, Ann Arbor.

Data availability

The chemical composition and predicted properties (surface energies, unstable stacking fault energies and ductility parameters) for 1184 screened alloys are available at Materials Commons with the following DOI: 10.13011/m3-kptn-e839.

Declarations

Conflict of interest

The authors declare that they have no conflict of interest.

Supplementary Information

The online version contains supplementary material available at https://doi.org/10.1557/s43579-022-00241-1.

References

1. D.B. Miracle, J.D. Miller, O.N. Senkov, C. Woodward, M.D. Uchic, J. Tiley, Exploration and development of high entropy alloys for structural applications. Entropy **16**, 494 (2014)
2. O. Senkov, J. Scott, S. Senkova, F. Meisenkothen, D. Miracle, C. Woodward, Microstructure and elevated temperature properties of a refractory TaNbHfZrTi alloy. J. Mater. Sci. **47**, 4062 (2012)
3. F. Maresca, W.A. Curtin, Mechanistic origin of high strength in refractory BCC high entropy alloys up to 1900 K. Acta Mater. **182**, 235 (2020)
4. G.R. Holcomb, C. Carney, Ö.N. Doğan, Oxidation of alloys for energy applications in supercritical CO_2 and H_2O. Corros. Sci. **109**, 22 (2016)
5. W. Zhang, Y. Qi, L. Zhang, Y. Tang, C. Qi, Q. Shen, Y. Ma, B. Wang, The effect of alloy elements on corrosion and oxidative resistance of W-based alloy films. Surf. Coat. Technol. **434**, 128165 (2022)
6. E. Mak, B. Yin, W. Curtin, A ductility criterion for BCC high entropy alloys. J. Mech. Phys. Solids **152**, 104389 (2021)
7. S. Pugh, XCII. Relations between the elastic moduli and the plastic properties of polycrystalline pure metals. Lond. Edinb. Dublin Philos. Mag. J. Sci. **45**, 823 (1954)
8. J.R. Rice, R. Thomson, Ductile versus brittle behaviour of crystals. Philos. Mag. J. Theor. Exp. Appl. Phys. **29**, 73 (1974)
9. J.R. Rice, Dislocation nucleation from a crack tip: an analysis based on the Peierls concept. J. Mech. Phys. Solids **40**, 239 (1992)
10. A. Zunger, S. Wei, L. Ferreira, J. Bernard, Special quasirandom structures. Phys. Rev. Lett. **65**, 353 (1990)
11. M. de Jong, L. Qi, D.L. Olmsted, A. van de Walle, M. Asta, Calculations of planar defect energies in substitutional alloys using the special-quasirandom-structure approach. Phys. Rev. B **93**, 094101 (2016)
12. Y.-J. Hu, A. Sundar, S. Ogata, L. Qi, Screening of generalized stacking fault energies, surface energies and intrinsic ductile potency of refractory multicomponent alloys. Acta Mater. **210**, 116800 (2021)

13. J.L. Johnson, Annealing of refractory metals, in *Heat Treating of Nonferrous Alloys* (ASM International, 2016) https://arxiv.org/abs/https://dl.asminternational.org/book/chapter-pdf/517852/a0006255.pdf, https://dl.asminternational.org/book/chapter-pdf/517852/a0006255.pdf. Accessed 10 Jul 2021
14. A. Van de Walle, P. Tiwary, M. De Jong, D. Olmsted, M. Asta, A. Dick, D. Shin, Y. Wang, L.-Q. Chen, Z.-K. Liu, Efficient stochastic generation of special quasirandom structures. CALPHAD **42**, 13 (2013)
15. G. Kresse, J. Hafner, Ab initio molecular dynamics for liquid metals. Phys. Rev. B **47**, 558 (1993)
16. G. Kresse, D. Joubert, From ultrasoft pseudopotentials to the projector augmented-wave method. Phys. Rev. B **59**, 1758 (1999)
17. P.E. Blöchl, Projector augmented-wave method. Phys. Rev. B **50**, 17953 (1994)
18. J.P. Perdew, K. Burke, M. Ernzerhof, Generalized gradient approximation made simple. Phys. Rev. Lett. **77**, 3865 (1996)
19. F. Pedregosa, G. Varoquaux, A. Gramfort, V. Michel, B. Thirion, O. Grisel, M. Blondel, P. Prettenhofer, R. Weiss, V. Dubourg, J. Vanderplas, A. Passos, D. Cournapeau, M. Brucher, M. Perrot, E. Duchesnay, Scikit-learn: machine learning in Python. J. Mach. Learn. Res. **12**, 2825 (2011)
20. Y.-J. Hu, G. Zhao, B. Zhang, C. Yang, M. Zhang, Z.-K. Liu, X. Qian, L. Qi, Local electronic descriptors for solute–defect interactions in BCC refractory metals. Nat. Commun. (2019). https://doi.org/10.1038/s41467-019-12452-7
21. J.-O. Andersson, T. Helander, L. Höglund, P. Shi, B. Sundman, Thermo-Calc & DICTRA, computational tools for materials science. CALPHAD **26**, 273 (2002)
22. U.R. Kattner, The CALPHAD method and its role in material and process development. Tecnol. metal. mater. miner. **13**, 3 (2016)
23. L. Qi, D. Chrzan, Tuning ideal tensile strengths and intrinsic ductility of BCC refractory alloys. Phys. Rev. Lett. **112**, 115503 (2014)
24. https://thermocalc.com/products/software-development-kits/tc-python/. Accessed Mar 2022
25. M. Esmaily, Y. Qiu, S. Bigdeli, M.B. Venkataraman, A. Allanore, N. Birbilis, High-temperature oxidation behaviour of AlxFeCrCoNi and AlTiVCr compositionally complex alloys. NPJ Mater. Degrad. **4**, 1 (2020)
26. P. Koukkari, R. Pajarre, Phase diagrams with the driving force and extent of reaction as axis variables. CALPHAD **74**, 102290 (2021)
27. C. Zhang, J. Zhu, H. Zheng, H. Li, S. Liu, G.J. Cheng, A review on microstructures and properties of high entropy alloys manufactured by selective laser melting. Int. J. Extreme Manuf. **2**, 032003 (2020)
28. X. Chen, Z. Liu, D. Wu, N. Cai, X. Sun, D.N. Zakharov, S. Hwang, D. Su, G. Wang, G. Zhou, Passive oxide film growth observed on the atomic scale. Adv. Mater. Interfaces **9**(11), 2102487 (2022)
29. A. Khalifeh, *Stress Corrosion Cracking Behavior of Materials* (IntechOpen, London, 2020)
30. D. Scheiber, R. Pippan, P. Puschnig, L. Romaner, Ab initio search for cohesion-enhancing impurity elements at grain boundaries in molybdenum and tungsten. Model. Simul. Mater. Sci. Eng. **24**, 085009 (2016)